

Novel $\text{CuIn}_{1-x}\text{Ga}_x\text{Te}_2$ Structures for High Efficiency Photo-electrochemical Solar Cells

M.M.S. Sanad*, M. M. Rashad, Atef Y. Shenouda

Central Metallurgical Research and Development Institute, P.O. Box: 87 Helwan, Cairo, Egypt

*E-mail: mustafa_sanad2002@yahoo.com

Received: 7 March 2016 / Accepted: 5 April 2016 / Published: 4 May 2016

Novel $\text{CuIn}_{1-x}\text{Ga}_x\text{Te}_2$ (CIGT; $x = 0, 0.3, 0.5$ and 0.7) chalcopyrite structures for photo-electrochemical solar cells have been successfully synthesized via a facile co-precipitation method. Briefly, tetragonal chalcopyrite structure was perceived with as-synthesized CIT sample whereas chalcopyrite phase was accompanied with minor impurity phases of cubic In_2O_3 and hexagonal Te metal with increasing the Ga^{3+} ion ratio. Meanwhile, a slight increase in the unit cell volume of chalcopyrite crystals was observed with the substitution In^{3+} ions with different ratios of Ga^{3+} ions. Moreover, the microstructure characteristics of the as-prepared chalcopyrite samples were exhibited different morphologies with different Ga^{3+} ion concentrations. Furthermore, the band gap energy and calculated refractive index were leaned on the Ga^{3+} ion content. Generally, the J-V characteristic measurements were coherently performed for the corresponding photo-electrochemical solar cells using the as-prepared photo-electrode materials. Accordingly, $\text{CuIn}_{0.3}\text{Ga}_{0.7}\text{Te}_2$ sample was displayed the highest photovoltaic performance with conversion efficiency (η) ~ 6.19 % and fill factor (FF) ~ 24.98 %, respectively. The superior power conversion performance was discussed based on the electrochemical impedance spectra (EIS) results which confirmed the enhanced electronic conductivities of the as-prepared photoelectrodes and exhibited well agreement with the obtained optical properties as well as J-V measurements.

Keywords: Chalcopyrite CIGT; Co-precipitation synthesis; Photovoltaic performance; Charge transfer resistance

1. INTRODUCTION

The significant global warming prospects, the limited fossil fuel reserves as well as the anticipated decline in cost make appeal for large scale exploitation of clean renewable energy sources such as wind and solar is greater than ever. Therefore, photo-electrochemical cell (PEC) and photovoltaic (PV) are becoming among the most proactive solutions for harvesting the solar energy [1]. This is because the light energy may be converted into electrical and/or chemical energy in such

photo-electrochemical (PEC) solar cells [2]. In other words, it is known that the performance and effectiveness of a solar cell device mainly depend upon its design and the properties of the photovoltaic materials included especially the light absorbers and their connections to the external circuit [3]. In particular, ternary CuInTe_2 chalcopyrite (CIT) has been extensively utilized as photoanodes in photo-electrochemical cells (PECs) and photovoltaics (PVs) due to their high absorption coefficients, optimal band gap energy and good photostability [4-7]. Accordingly, a lot of synthetic strategies have been reported to prepare CuInTe_2 powders including melt-quenching [8], sol-gel [9], hydrothermal [10], solvothermal [11] and microwave methods [12, 13], as well as CuInTe_2 thin films were formed using different pathways including thermal evaporation [14, 15], graphite box annealing-rapid cooling [16], chemical vapor transport [17], molecular beam epitaxy co-evaporation [18] and electrodeposition techniques [19]. Besides, a plenty of studies are investigated the ionic substitution of In^{3+} ion by different metal and non-metal ions such as Ga^{3+} [15, 20, 21], Ce^{3+} [22], Eu^{3+} [23] and Sm^{3+} [24] and B^{3+} [25] in order to improve the power conversion efficiency of solar cells.

Herein, in the present work, we have developed a new facile co-precipitation method to synthesize micron and sub-micron sized $\text{CuIn}_{1-x}\text{Ga}_x\text{Te}_2$ particles ($x = 0, 0.3, 0.5$ and 0.7) using NaBH_4 as reducing agent mainly for the first time.

Thereby, the as-prepared CIT and CIGT compounds of novel morphologies were fully characterized using X-ray diffraction analysis (XRD) and field emission scanning electron microscopy (FE-SEM). Meanwhile, the effect of Ga^{3+} ion substitution on the structural and optical properties of semiconducting powders was also studied. Furthermore, the photovoltaic performance, conversion efficiency and charge transfer resistance of the fabricated cells were extensively examined as well.

2. EXPERIMENTAL

2.1. Materials

All the chemicals used in this study such as (copper (I) chloride CuCl Sigma-Aldrich-99.9%, indium nitrate hydrate $\text{In}(\text{NO}_3)_3 \cdot x\text{H}_2\text{O}$ Aldrich-99.9%, tellurium (IV) chloride TeCl_4 Strem Chemicals-99.9%, gallium nitrate hydrate $\text{Ga}(\text{NO}_3)_3 \cdot x\text{H}_2\text{O}$ Sigma-Aldrich-99.9%, sodium borohydride NaBH_4 Sigma-Aldrich-99.9% and sodium hydroxide NaOH Sigma-Aldrich -98.9%) were of analytical grade. Deionized water was used in the whole work.

2.2. Preparation of light absorbing materials

$\text{CuIn}_{1-x}\text{Ga}_x\text{Te}_2$ precursors ($x = 0, 0.3, 0.5$ and 0.7) have been prepared by mixing stoichiometric amounts of Cu^+ , In^{3+} , Ga^{3+} and Te^{4+} solutions, respectively. The pH value of the solution was adjusted at the range 10-11 using 0.5 M NaOH as a base. The precipitated hydroxide precursors were stirred gently for 15 min to achieve a good homogeneity and to attain a stable pH conditions. After that, a suitable amount of NaBH_4 solution was added to the mixture to reduce the hydroxide phase to the metalloid alloy. After that, the mixture was stirred with heating at around 85°C for 2 h. Then, the solution mixture was left overnight to cool and precipitate the metalloid alloy compound by

decantation. Thereafter, the precipitated powder was filtered out and washed by 1% of NaBH_4 solution followed by distilled water. Finally, the prepared powders were annealed at $350\text{ }^\circ\text{C}$ for 2 h in Argon/ H_2 (5%) atmosphere.

2.3. Fabrication of photo-electrochemical cells (PECs)

2.3.1. Preparation of photoanodes

The photoanode materials were fabricated by intimately mixing the active material (95 wt%) $\text{CuIn}_{1-x}\text{Ga}_x\text{Te}_2$, and polyvinylidene fluoride, PVDF (5 wt%) as a binder. Then, the powder mixture was dissolved in N-methyl-2-pyrrolidone, NMP to form a colloid slurry paste. The mixed slurry was plated onto a conducting glass substrate coated with a thin film of indium tin oxide (ITO glass) using drop coating technique. The mass loading of active materials was 7 mg/cm^2 in the examined electrode. The coated ITO glass electrodes were dried under vacuum at $80\text{ }^\circ\text{C}$ overnight.

2.3.2. Construction of PECs

The coated ITO glass acting as the working electrode against glassy carbon counter/ reference electrode was immersed in an electrolyte of iodine in potassium iodide. The active area of working electrode was $3\text{ cm} \times 1.5\text{ cm}$. The solar cell configuration was arranged: conducting ITO glass/ $\text{CuIn}_{1-x}\text{Ga}_x\text{Te}_2$ / $0.5\text{ M KI} + 0.5\text{ M I}_2$ / C as shown in Fig. 1.

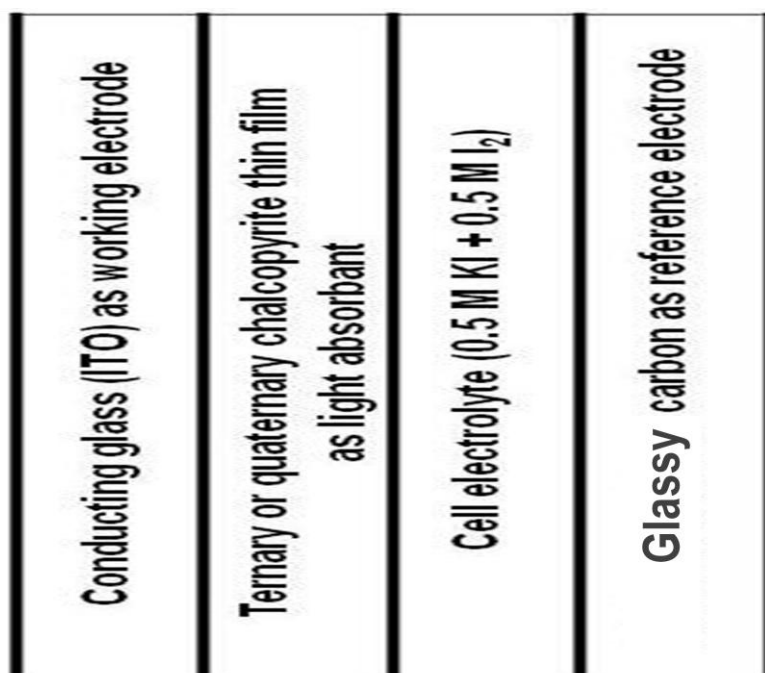


Figure 1. Schematic diagram for Photo-electrochemical (PEC) solar cell configuration under illumination

2.4. Characterization techniques

2.4.1. Physical characterization

The crystalline phases of different samples were identified by X-ray diffraction (XRD) using a step size of 0.02° and at a scanning rate of $0.16^\circ/\text{min}$ on a Bruker axis D8 diffractometer with crystallographic data software Topas 2 using Cu $K\alpha$ ($\lambda = 1.54056 \text{ \AA}$) radiation operating at accelerating voltage and applied current were 40 kV and 80 mA, respectively. The diffraction data was recorded for 2θ values between 10° and 80° . The particle morphology was inspected with a scanning electron microscope FE-SEM (JEOL-JSM-5410 Japan). The optical measurements were implemented using UV-Vis-NIR scanning spectrophotometer (Perkin Elmer Lambda 1050 Spectrophotometer, USA) using 1 cm path length quartz cell.

2.4.2. Photovoltaic characterization

Photocurrent-voltage J - V characteristic curves measurements were performed using the solar simulator Sciencetech SS150W- AAA. Light intensity of Xenon arc lamp (150 W) was adjusted at 100 mW/cm^2 using Air Mass 1.5 Global Filter. The calibrated reference cell consists of 20 x 20 mm monocrystalline silicon (model SC-LT) photovoltaic cell encased in 92 x 70 x 16 mm metal enclosure with a protective quartz window. The reference detector (SSIIVT-refl) is effective in sensing wavelengths between 190 and 1100 nm and it is calibrated with the 1 Sun. The 1 Sun AM1.5 simulated sunlight reference spectrum according to an ASTM G173 standard was used. Solar decay and I- V curves were measured by Keithley 2400 multimeter connected to a computer and software. Parameters measured by I- V Software were open circuit voltage (V_{oc}), short circuit current (I_{sc}), maximum power (P_{in}) and filling factor (FF).

2.4.3. Electrochemical measurements

EIS measurements were accomplished for the fabricated photo-electrochemical cells under dark conditions using potentiostat (Parostat 4000 Princeton, USA). The impedance measurements amplitude was 20 mV and the frequency range was 1MHz-10 mHz.

3. RESULTS AND DISCUSSION

3.1. Crystal structure

Fig.2 evinces XRD patterns of the as-synthesized $\text{CuIn}_{1-x}\text{Ga}_x\text{Te}_2$ ($x = 0, 0.3, 0.5$ and 0.7) powders. The main diffraction peaks of (112), (204), (312), (325/332) and (228/424) elucidated the chalcopyrite phase tetragonal structure (ICDD # 81-1937) at diffraction angles 24.85° , 41.14° , 48.75° , 65.57° and 74.98° , respectively were indexed. However, XRD data indicated the presence of minor

amounts of cubic In₂O₃ (ICDD 44-1087) and hexagonal Te metal phases (ICDD 78-2312) as secondary phases at x = 0.3, 0.5 and 0.7.

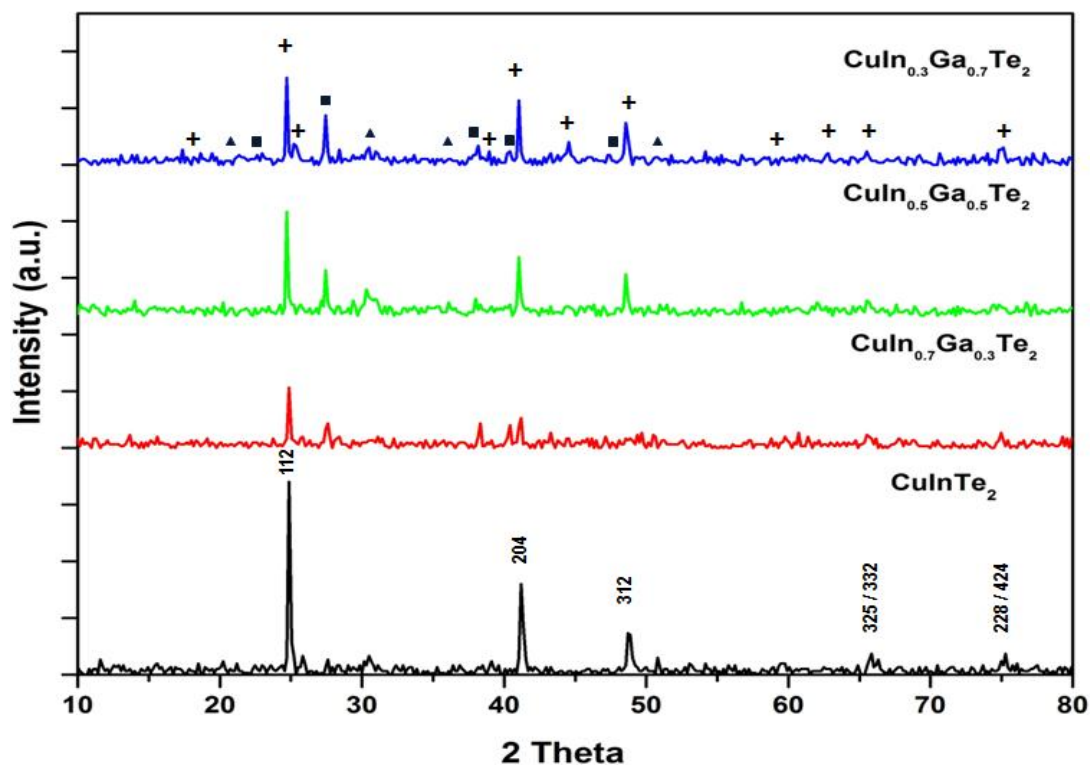


Figure 2. XRD patterns of the as-synthesized CuIn_{1-x}Ga_xTe₂ at different (x) values (0, 0.3, 0.5 and 0.7) [CuInTe₂ (+), In₂O₃ (▲) and Te metal (■)]

The crystallite size of CuIn_{1-x}Ga_xTe₂ phases was calculated for the most intense peak of (112) plane from X-ray pattern based on Debye-Scherrer formula [26].

$$D = \frac{K\lambda}{\beta \cos\theta} \tag{1}$$

Where *D* = average crystallite size, *K*= geometric factor (0.98), *λ* = X-ray wavelength (0.154 nm), *β* = FWHM of the diffraction peak (in radian) and *θ* = diffraction angle.

Table 1. Crystallographic features of CuIn_{1-x}Ga_xTe₂ samples annealed at 350 °C for 2 h

CuIn _{1-x} Ga _x Te ₂	Crystallite size (nm)	<i>a</i> (Å)	<i>c</i> (Å)	<i>c/a</i> (Å)	<i>V</i> _{Cell} (Å ³)
CuInTe ₂	110.7	6.20	12.36	1.990	475.65
CuIn _{0.7} Ga _{0.3} Te ₂	110.9	6.21	12.39	1.996	477.56
CuIn _{0.5} Ga _{0.5} Te ₂	105.6	6.22	12.38	1.992	478.19
CuIn _{0.3} Ga _{0.7} Te ₂	111.2	6.22	12.37	1.989	478.13

The average crystallite size of pure CuInTe₂ powder was 110.7 nm, as depicted in Table 1. Evidently, it was found that the crystallite size values of 30 and 70% Ga³⁺-doped samples were slightly increased into 110.9 and 111.2 nm due to the growth enhancement of particles. Meanwhile, the crystallite size value of 50 % Ga³⁺ ion content was slightly decreased into 105.6 nm. This lowering in crystallite size might be attributed to the larger extent of secondary phases which cause the imperfect growth of CuInTe₂ particles.

The lattice spacing is calculated using the Bragg’s formula [27]:

$$d = \frac{\lambda}{2 \sin\theta} \tag{2}$$

Therefore, the lattice parameters (*a*, *c*) and unit cell volume (*V_{Cell}*) for the tetragonal are determined using the following relations [28]:

$$\frac{1}{d} = \sqrt{\frac{h^2+k^2}{a^2}} + \sqrt{\frac{l^2}{c^2}} \tag{3}$$

$$V_{Cell} = a^2 \times c \tag{4}$$

Obviously, one can note that the substitution In³⁺ ions with different ratios of Ga³⁺ ions causes a noticeable increase in the unit cell volume of chalcopyrite crystals as shown in Fig. 3.

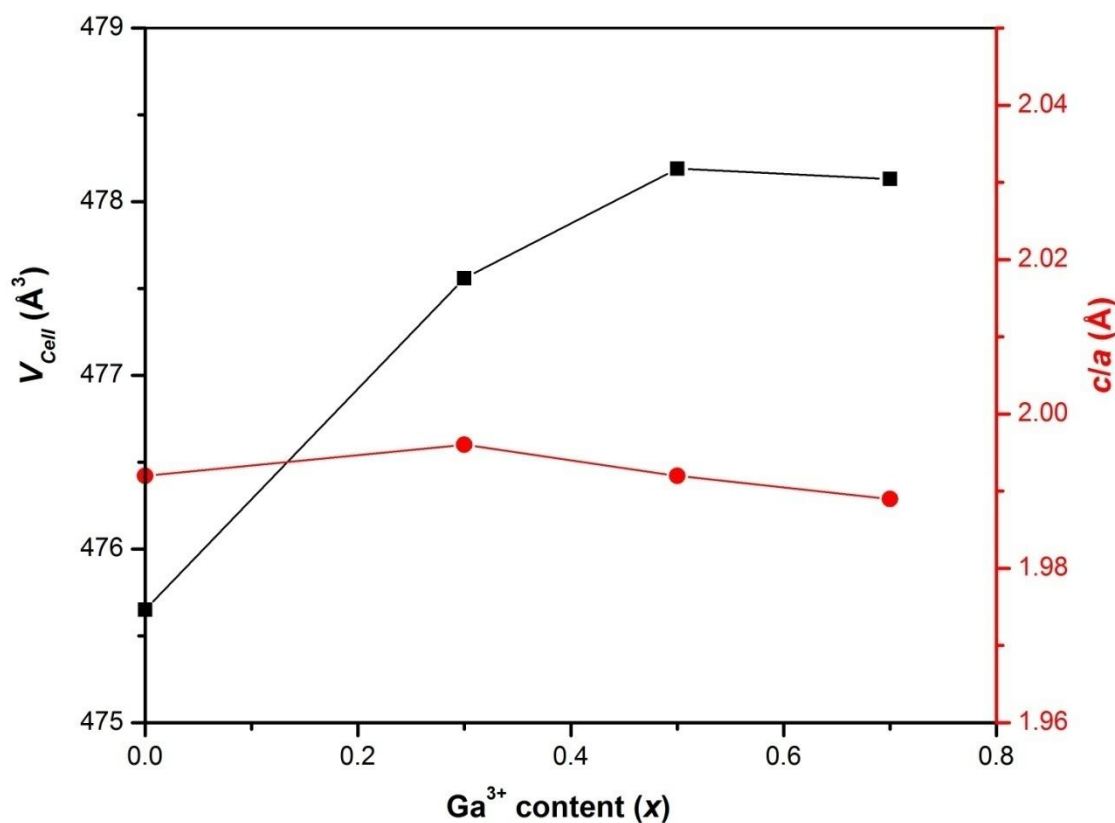


Figure 3. Effect of Ga³⁺ ion content on different unit cell parameters of CuIn_{1-x}Ga_xTe₂ powders

However, Vegard’s law states that the lattice constant “*c*” should be a linear function of the composition variable *x*. Therefore, the calculated lattice parameters for each composition of CuIn_{1-x}

$x\text{Ga}_x\text{Te}_2$ are given in Table 1. Indium ($r = 62 \text{ pm}$) has a relatively larger ionic radius “ r ” than gallium “ $r = 47 \text{ pm}$ ”. Hence, the lattice parameter “ c ” of the CIGT alloys was increased with increasing In^{3+} ion content. Moreover, another detectable decrease is estimated in c/a ratio from $x = 0.3$ to 0.7 which confirms the formation of a homogeneous alloy structure. In other words, values of the lattice parameter “ c ” increase linearly with decreasing gallium composition (increasing indium composition) and vice versa in case of lattice parameter “ a ” [29]. Generally, all such crystallographic features were summarized in Table 1.

3.2. Crystal morphology

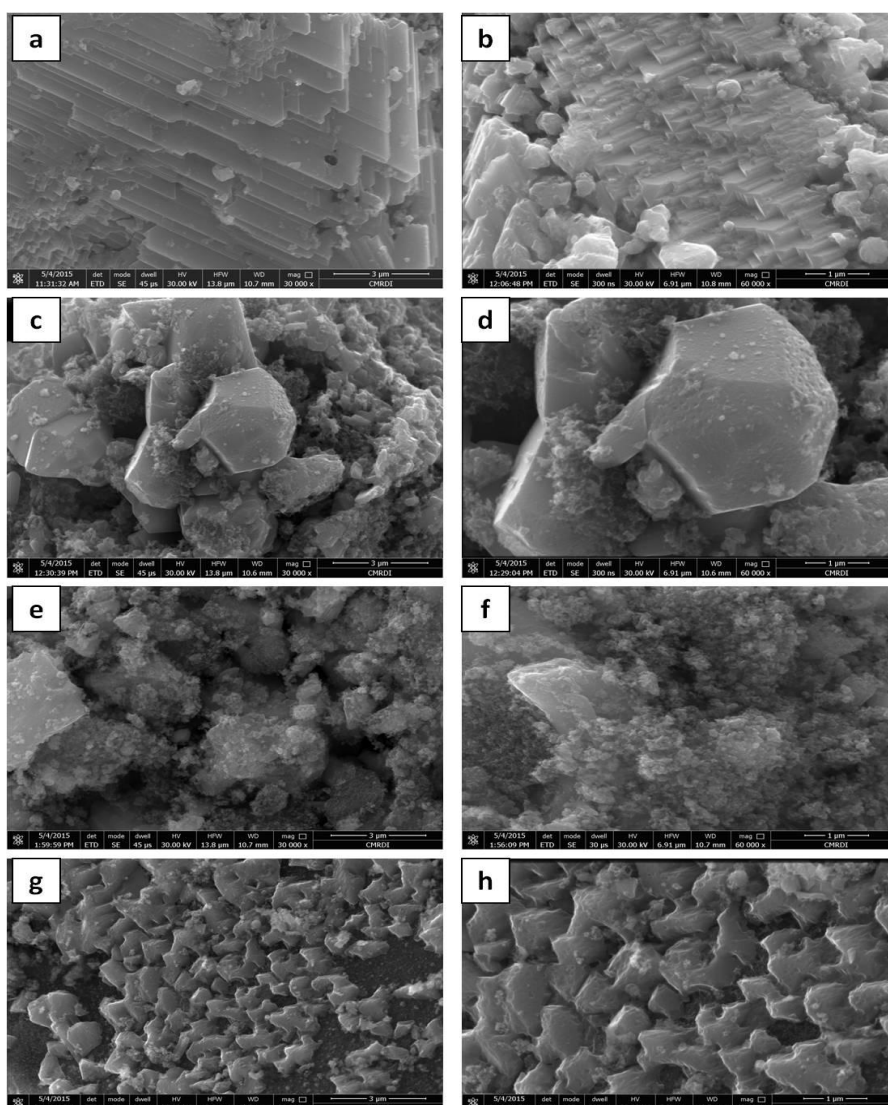


Figure 4. Crystal morphology of the as-synthesized CIT and CIGT powders at different gallium ratios (a, b) $x = 0$ (c, d) $x = 0.3$, (e, f) $x = 0.5$ and (g, h) $x = 0.7$

The microstructure characteristics of the as-prepared chalcopyrite samples were explored by FE-SEM images at low and high magnifications (30000 and 60000 X) as displayed in Fig. 4 (a-h). The particles of pure CIT exhibited a homogeneous closed-packed structures consisting of

uniform arrays of triangular prisms with facet planes as shown in Fig. 2 (a, b). It has an average particle size of 2-3 μm as well. However, two different types of morphology are clearly observed at Ga^{3+} ion molar ratio 0.3 as depicted in Fig. 4 (c, d).

Therefore, the small tetragonal crystals of average particle size $\sim 0.5 - 1.0 \mu\text{m}$ (corresponding to CIT particles) are found to be embedded between the large hexagonal crystals of average particle size $\sim 3-5 \mu\text{m}$ (corresponding to Te metal particles). Moreover, at 50% of Ga^{3+} ion content, the dense particles morphology exhibited indistinct and irregular shapes of quite spherical-like crystals with smaller particles size range (0.2 - 0.3 μm) as illustrated in Fig. 4 (e, f). Furthermore, at high Ga^{3+} ion content (70%), the particles are slightly converted into the clear triangular pyramidal-like crystals of particles size range $\sim 0.5 - 1.0 \mu\text{m}$ as seen in Fig. 4 (g, h).

Consequently, the obtained FE-SEM investigations for the particle morphology and size of the as-prepared CIT and CIGT samples are in good accordance with the previous XRD results.

3.3. Optical properties

3.3.1. Band gap energy

Table 2. Optical properties of $\text{CuIn}_{1-x}\text{Ga}_x\text{Te}_2$ samples annealed at 350 $^\circ\text{C}$ for 2 h

$\text{CuIn}_{1-x}\text{Ga}_x\text{Te}_2$	Band gap energy E_g (eV)	Calculated refractive index (n)
CuInTe_2	1.39	2.88
$\text{CuIn}_{0.7}\text{Ga}_{0.3}\text{Te}_2$	1.71	2.73
$\text{CuIn}_{0.5}\text{Ga}_{0.5}\text{Te}_2$	1.79	2.70
$\text{CuIn}_{0.3}\text{Ga}_{0.7}\text{Te}_2$	1.40	2.87

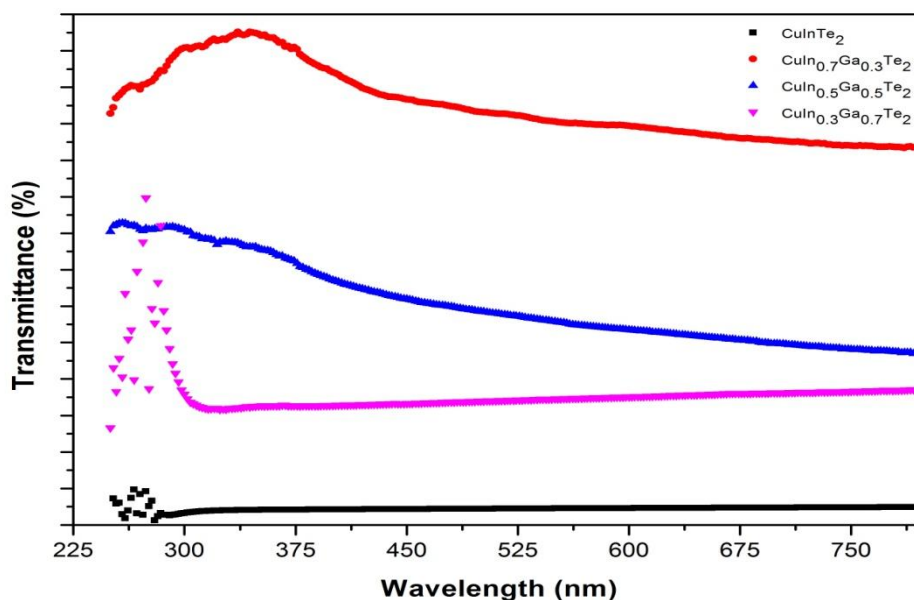


Figure 5. (a): Transmittance spectra of the as-synthesized CIT and CIGT powders

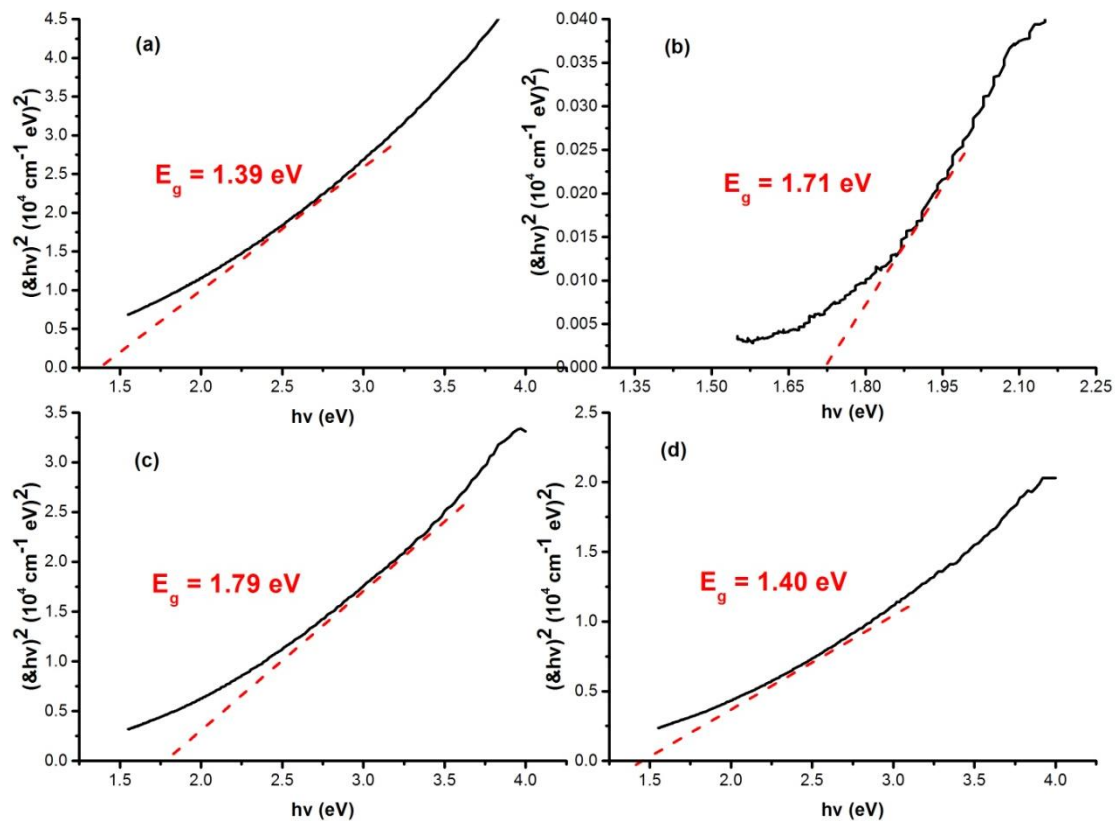


Figure 5. (b): Optical band gap energy of the as-synthesized CIT and CIGT powders at different gallium ratios (a) $x = 0$ (b) $x = 0.3$, (c) $x = 0.5$ and (d) $x = 0.7$

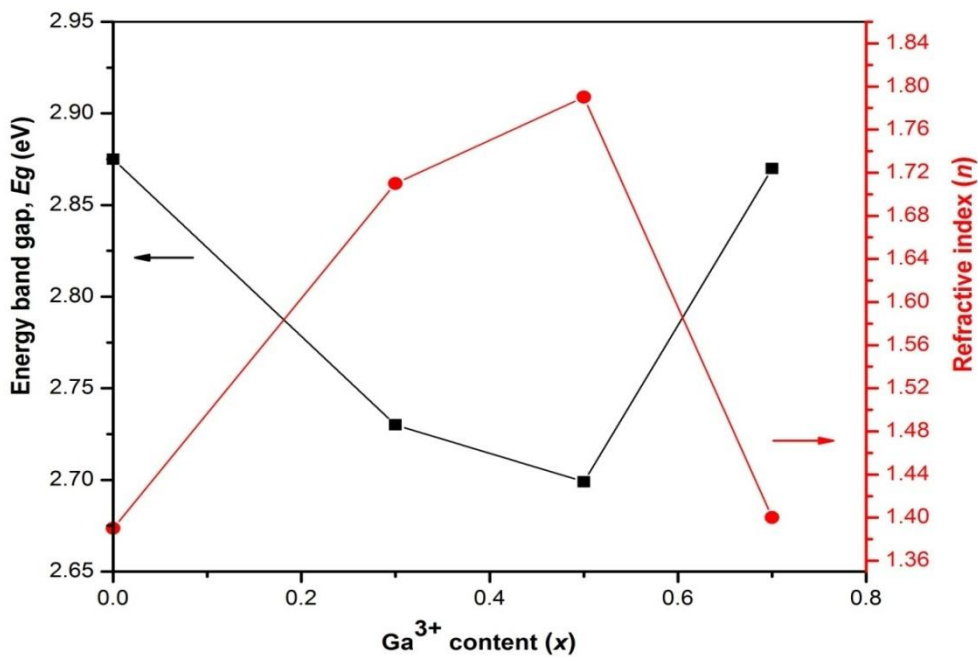


Figure 5. (c): Optical band gap energy versus the calculated refractive indices of $\text{CuIn}_{1-x}\text{Ga}_x\text{Te}_2$ powders

The optical properties of the synthesized CIT and CIGT particles are examined by UV-Vis spectrophotometer using integrating sphere unit and the obtained band gap energy results are listed in Table. 2. For the measurement, the synthesized powders are well dispersed in distilled water and the resultant solutions were used for the measurement.

Specular transmittance measurements of $\text{CuIn}_{1-x}\text{Ga}_x\text{Te}_2$ samples have been carried out using UV-Vis-NIR Perkin Elmer Lambda 1050 Spectrophotometer in the wavelength range 250-800 nm at room temperature as shown in Fig. 5 (a).

Mainly, the transmission spectra are occurred between wavelength range 245 and 375 nm for these samples.

The optical absorbance A and the optical absorption coefficient “ α ” have been obtained using the following relations [30, 31]:

$$\text{Log}(1/T) = \alpha t \quad (5)$$

$$\text{The absorbance } A = \text{Log}(I^\circ/I) = \alpha t \quad (6)$$

$$\text{Transmittance \% } T = 100(I^\circ/I) \quad (7)$$

Where T is the transmittance of the spectra, t is the film thickness,

I° and I are the intensities of the incident and passed light through the sample.

Analysis of optical absorption spectra is one of the most productive tools for determining optical band gap of the film. Therefore, the band gap energy was determined by extrapolating the absorption coefficient (α) to zero from the spectral data.

The absorption coefficient was calculated by the following equation

$$(\alpha h\nu)^m = h\nu - E_g \quad (8)$$

Where α is the absorption coefficient, $h\nu$ is the photon energy, E_g is the band gap energy, $m = 1/2$ or $3/2$ for indirect allowed and indirect forbidden transitions, and $m = 2$ or 3 for direct allowed and direct forbidden transitions. Evidently, band gaps are calculated by plotting $(\alpha h\nu)^2$ against $h\nu$ and extrapolating the linear portion of the curve on $h\nu$ axis to $\alpha = 0$ as shown in Fig. 5(b). It is found that pure CIT and CIGT (70% Ga^{3+}) have lower E_g values than those of CIGT samples at all 30 and 50% of Ga^{3+} content. For instance, it is also seen that the E_g value increased with decreasing ionic radius of doping ion (i.e. $\text{Ga}^{3+} < \text{In}^{3+}$) [32, 33]. Overall, the measured E_g values were in good agreement with the other previous reports [14, 23, 24, 34].

3.3.2. Refractive index

The refractive index (n) of semiconducting materials is very important in determining the optical properties of the material. Knowledge of n is essential to design heterostructure lasers in optoelectronic devices as well as in solar cell applications. The refractive index (n) of the samples can be calculated using Moss relation [35], where E_g is the energy band gap.

$$E_g n_f^4 = 95 \text{ eV} \quad (9)$$

The calculated averages of the refractive index for CIT and CIGT samples are listed in Table 2. Fig. 5 (c) shows the variation in the refractive indices against the band gap energies. It is indicated that the maximum refractive index (n) is about 2.875 at 1.39 eV for pure CIT. Moreover, it can be implied

that the refractive indices are shifted towards lower values at higher E_g values. Such obtained results confirmed that the change in the refractive indices is mainly dependent on the absorption features of the semiconductors [33, 35, 36].

3.4. Photovoltaic Characteristics

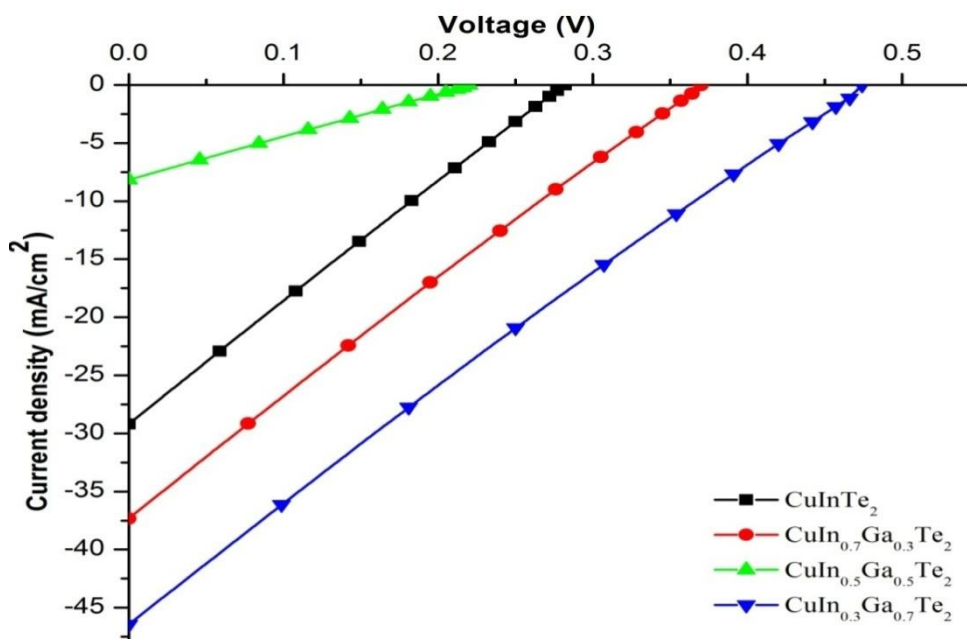


Figure 6. J–V plots of the photo-electrochemical cells of $\text{CuIn}_{1-x}\text{Ga}_x\text{Te}_2$ samples

The total photoelectric conversion efficiency (η) was calculated according to Eq. (11):

$$\eta \% = \frac{P_{\max}}{P_{\text{in}} \cdot A} \cdot 100 = \frac{J_{\text{sc}} \cdot V_{\text{oc}} \cdot \text{FF}}{P_{\text{in}} \cdot A} \cdot 100 \quad (11)$$

Where, open circuit voltage (V_{oc}), short circuit current (J_{sc}), maximum power (P_{\max}), filling factor (FF), the light intensity ($100 \text{ mW/cm}^2 = 1 \text{ Sun}$) of the incident monochromatic light (P_{in}) and (A) active area of thin film.

The fill factor (FF) is the ratio between the maximum output power density available ($J_m \cdot V_m$) which given from the maximum power combining short-circuit and open-circuit situations (Eq. 2) and it describes the “squareness” of the J-V curve.

$$\text{FF} (\%) = \frac{J_m \cdot V_m}{J_{\text{sc}} \cdot V_{\text{oc}}} \cdot 100 \quad (12)$$

Where, (V_m) is maximum voltage and (J_m) is maximum current. The measurements were repeated three times for each sample, and the experimental error was found to be within ca. 5%.

Fig. 6 shows the I-V characteristics of the fabricated photoelectrochemical solar cells under illumination conditions. The corresponding basic solar cell parameters are summarized in Table 3.

Table 3. J–V characteristics of the photo-electrochemical cells of CuIn_{1-x}Ga_xTe₂ samples

Anode materials	V _{max}	J _{max} (mA/cm ²)	V _{oc}	J _{sc} (mA/cm ²)	FF(%)	η (%) per unit area	Active area (cm ²)	R _{bulk} (Ω)
CuInTe ₂	0.14	15	0.282	29.198	25.5045	2.36	4.0	0.0093
CuIn _{0.7} Ga _{0.3} Te ₂	0.175	19	0.37	37.321	24.0789	3.74	4.0	0.0092
CuIn _{0.5} Ga _{0.5} Te ₂	0.09	5	0.22	8.159	25.0699	0.51	4.0	0.018
CuIn _{0.3} Ga _{0.7} Te ₂	0.25	22	0.474	46.451	24.9798	6.19	4.0	0.0114

Obviously, the correlation between the photovoltaic performance parameters and the effect of In³⁺ ion substitution by different Ga³⁺ ion contents in the pure chalcopyrite CIT sample was evidenced. The short-circuit currents (*J*_{sc}) and open-circuit voltage (*V*_{oc}) of the PECs were in the range 8.16–46.45 mA cm⁻² and 0.22–0.47 V, respectively. It can be noted that CuIn_{0.3}Ga_{0.7}Te₂ sample gave the highest overall conversion efficiency (η) ~ 6.19 % and lowest fill factor (FF) ~ 24.98 %, respectively at total active area 4.0 cm². The reason was based on the fact that the decrease of band gap energy of the absorber efficiently enhances the charge separations and light absorption resulting in a significant improvement in the solar cell performance [37]. On the other hand, the bulk resistance of anode materials can be obtained from the following relation:

$$R_{\text{bulk}} = \frac{V_{\text{max}}}{J_{\text{max}}} \quad (13)$$

3.5. Electrochemical impedance spectroscopy (EIS) analysis

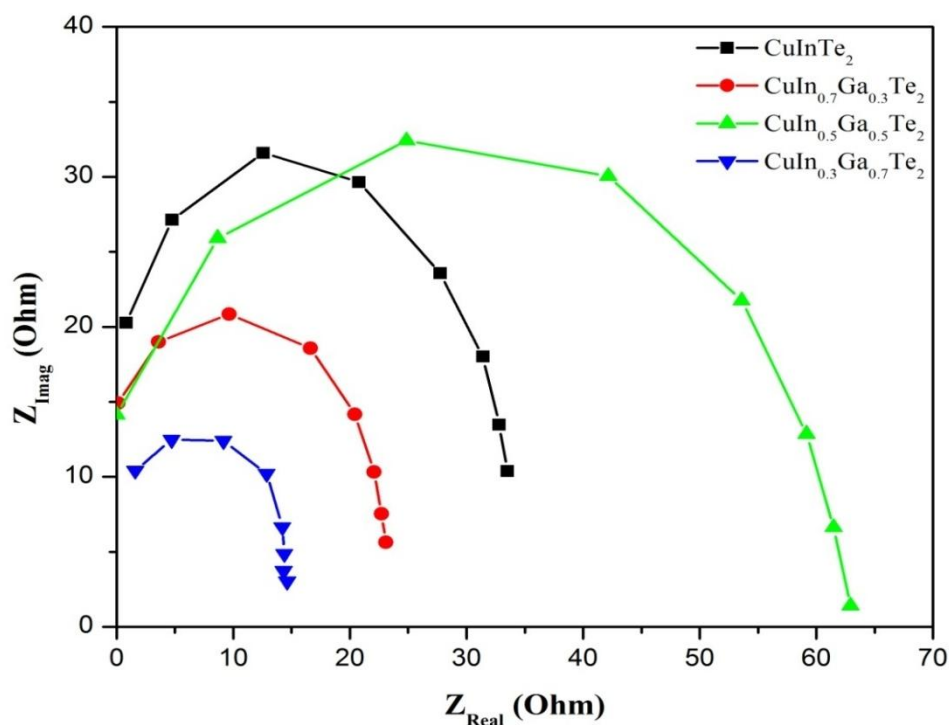


Figure 7. (a): Nyquist plots of the as-prepared CIT and CIGT photoelectrode materials at different Ga³⁺ ion concentrations in the three electrode cell

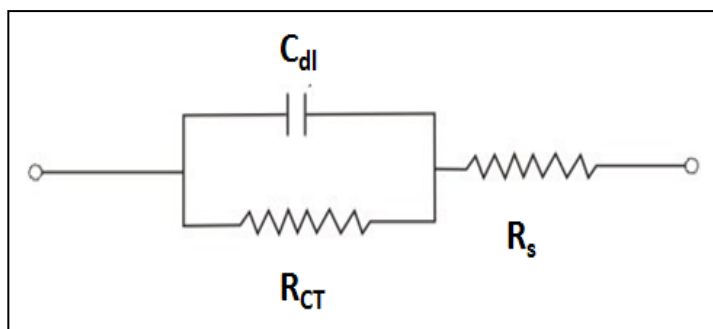


Figure 7. (b): Equivalent circuit of the EIS model

The EIS graph is given in Fig. 7 (a). The impedance of four kinds of photoelectrodes are carefully studied using Nyquist plot in order to investigate the electron transfer at the ITO/CuIn_{1-x}Ga_xTe₂/electrolyte interface. Fig. 7 (b) shows the equivalent circuit that composed of a solution resistor with resistance (R_s), an electrode-electrolyte interfacial charge transfer resistance (R_{CT}) and a double layer capacitor (C_{dl}). R_s value was obtained from the fitting as the intercept on the real axis of the high frequency range and R_{CT} was estimated from the diameter of the semicircle. R_s , R_{CT} , and other fitting parameters are summarized in Table 4.

Table 4. Fitting parameters of the experimental impedance spectroscopy data

CuIn _{1-x} Ga _x Te ₂	R_s (Ω)	R_{CT} (Ω)	C_{dl} (F)
CuInTe ₂	0.827	32.42	9.795×10^{-9}
CuIn _{0.7} Ga _{0.3} Te ₂	0.143	23.19	1.369×10^{-8}
CuIn _{0.5} Ga _{0.5} Te ₂	0.003	62.38	1.279×10^{-8}
CuIn _{0.3} Ga _{0.7} Te ₂	1.597	13.28	1.899×10^{-8}

It is observed that CuIn_{0.3}Ga_{0.7}Te₂ has the lowest charge transfer resistance in comparison with the other samples. Consequently, the EIS data showed an explanation based on the charge transfer resistance, which was consistently coincided with the I-V measurements.

4. CONCLUSION

Novel highly ordered chalcopyrite structures were prepared from simple co-precipitation method to be implemented as high performance photoanode materials in PEC solar devices. The crystallographic and morphological features were easily controlled by varying the In³⁺/Ga³⁺ molar ratio. The as-prepared CuIn_{1-x}Ga_xTe₂ showed tunable band gap energy and refractive index values especially that mainly depend on the absorption characteristics of photoelectrode materials. The highest conversion efficiency (η) ~ 6.19% and lowest fill factor (FF) ~ 24.98% have been accomplished for the fabricated PEC solar cell of chemical composition CuIn_{0.3}Ga_{0.7}Te₂. As

anticipated, the enhanced transport of photogenerated electrons has been achieved as a result of the microstructure; band gap energy (i.e. trap density) as well as the internal resistance minimization was responsible for the high photovoltaic performance.

References

1. M. Gratzel, *Phil. Trans. R. Soc. A* 365 (2007) 993.
2. S. Licht, Photoelectrochemical Solar Energy Storage Cells, Encyclopedia of Electrochemistry, 2007 Wiley-VCH Verlag GmbH & Co. KGaA DOI: 10.1002/9783527610426.bard060402.
3. J. Nelson, The Physics of Solar Cells, World Scientific Publishing Co Pte Ltd., ISBN: 978-1-86094-340-9, 2003, pp. 1-384,
4. D. Xue, K. Betzler and H. Hesse, *Phys. Rev. B*, 62 (2000) 13546.
5. T. Mise and T. Nakada, *Thin Solid Films*, 518 (2010) 5604.
6. S. Kim, M. Kang, S. Kim, J. Heo, J.H. Noh, S.H. Im, S.I. Seok and S.-W. Kim, *Nano*, 7 (2013) 4756.
7. J.F. Guillemoles, L. Kronik, D. Cahen, U. Rau, A. Jasenek and H.W. Schock, *J. Phys. Chem. B*, 104 (2000) 4849.
8. C. Rangasami, M. Jain and S. Kasiviswanathan, *AIP Conf. Proc.*, 1349 (2011) 1093.
9. S.J. Ahn, K. Kim, Y.G. Chun and K.H. Yoon, *Thin Solid Films*, 515 (2007) 4036.
10. S. Sukan, K. Baskar and R. Dhanasekaran, *Curr. Appl. Phys.*, 14 (2014) 1416.
11. C. Kim, D.H. Kim, Y.S. Son, H. Kim, J.Y. Bae and Y.S. Han, *Mater. Res. Bull.*, 47 (2012) 4054.
12. C.C. Landry, J. Lockwood and A.R. Barron, *Chem. Mater.*, 7 (1995) 699.
13. H. Grisar, O. Palchik, A. Gedanken, V. Palchik, M.A. Slifkin and A.M. Weiss, *Inorg. Chem.*, 42 (2003) 7148.
14. R. Diaz, M. Leon and F. Rueda, *J. Vac. Sci. Technol. A*, 10 (1992) 295.
15. Y. Atasoy, B.M. Basol, I. Polat, M. Tomakin, M. Parlak and E. Bacaksiz, *Thin Solid Films*, 592 (2015) 189.
16. S. Roy, P. Guha, S. Chaudhuri and A.K. Pal, *Vacuum*, 65 (2002) 27.
17. P. Prabukanthan and R. Dhanasekaran, *Mater. Res. Bull.*, 43 (2008) 1996.
18. T. Mise and T. Nakada, *Thin Solid Films*, 518 (2010) 5604.
19. D. Prasher, K. Dhakad, A.k. Sharma, V. Thakur and P. Rajaram, *Inter. J. Mater. Sci. Appl.*, 3 (2014) 1.
20. R. Dlar, J.M. Merino, F. Rueda and M. Leon, *J. Phys. D: Appl. Phys.*, 28 (1995) 1162.
21. I.V. Bodnar, *Technic. Phys.*, 48 (2003) 587.
22. F. Li and G. Yong-Quan, *Chin. Phys. B*, 23 (2014) 127801.
23. X. Nie and Y. Guo, *J. Solid State Chem.*, 233 (2016) 211.
24. X. Nie and Y. Guo, *Adv. Mater. Res.*, 1094 (2015) 218.
25. P. Termsaithong and A. Tubtimtae, *Mater. Lett.*, 138 (2015) 41.
26. U.S. Senapati and D. Sarkar, *Ind. J. Phys.*, 88 (2014) 557.
27. U.S. Senapati, D.K. Jha and D. Sarkar, *Res. J. Phys. Sci.*, 1 (2013) 1.
28. F. De Flaviis, N.G. Alexopoulos and O.M. Stafsudd, Microwave Theory and Techniques, *IEEE Trans.* 45 (1997) 963.
29. S.N. Malik, S. Mahboob, N. Haider, M.A. Malika and P. O'Brien, *Nanoscale*, 3 (2011) 5132.
30. R.M. Oksuzoglu, P. Bilgic, M. Yildirim and O. Deniz, *Opt. Laser Technol.*, 48 (2013) 102.
31. A.Y. Shenouda, M.M. Rashad and L. Chow, *J. Alloy. Compd.*, 563 (2013) 39.
32. Z. Zou, J. Ye and H. Arakawa, *Chem. Mater.*, 13 (2001) 1765.
33. Z. Xian-Zhou, S. Ke-Sheng, J. Zhao-Yong and H. Xiao-Fen, *Comput. Theor. Chem.*, 1010 (2013) 67.
34. B. Kuhn, W. Kaefer, K. Fess, K. Friemelt, C. Turner, M. Wendl and E. Bucher, *Phys. Status Solidi*

A, 162 (1997) 661.

35. N.M. Ravindra, P. Ganapathy and J. Choi, *Infrared Phys. Technol.*, 50 (2007) 21.

36. M. Boustani, K. El Assali, T. Bekkay and A. Khiara, *Sol. Energ. Mater. Sol. C.*, 45 (1997) 369.

37. T.K. Todorov, O. Gunawan, T. Gokmen and D. B. Mitzi, *Prog. Photovolt: Res. Appl.*, 21 (2013) 82.

© 2016 The Authors. Published by ESG (www.electrochemsci.org). This article is an open access article distributed under the terms and conditions of the Creative Commons Attribution license (<http://creativecommons.org/licenses/by/4.0/>).